IEEE Access
Multidisciplinary ⋮ Rapid Review ⋮ Open Access Journal

Received July 20, 2020, accepted August 3, 2020, date of publication August 10, 2020, date of current version August 21, 2020.

Digital Object Identifier 10.1109/ACCESS.2020.3015601

Analytical Model of Air-Gap Field in Hybrid Excitation and Interior Permanent Magnet Machine for Electric Logistics Vehicles

WENJING HU[1], XUEYI ZHANG[1], YULONG LEI[2], QINJUN DU[3], LIWEI SHI[1], AND GUODONG LIU[1]

[1]School of Transportation and Vehicle Engineering, Shandong University of Technology, Zibo 255049, China
[2]State Key Laboratory of Automotive Simulation and Control, Jilin University, Changchun 130022, China
[3]School of Electrical and Electronic Engineering, Shandong University of Technology, Zibo 255049, China

Corresponding author: Xueyi Zhang (zhangxueyi@sdut.edu.cn)

This work was supported by the National Natural Science Foundation of China under Grant 51875327 and Grant 51975340.

ABSTRACT With the increasing energy shortages and environmental degradation, electric logistics vehicle (ELVs) with energy conservation and environmental protection has become a research hotspot. The design of machine is the key to develop ELVs. Magnetic field analysis is the most critical issue since its accuracy affects the calculation of motor torque, loss, and other characteristics. To provide a calculation method for the field and performance analysis of the machine for ELVs, this paper presents an analytical model of air-gap field for hybrid excitation and interior permanent magnet machine. In the proposed model, it is taken into account for the shape of the stator and rotor teeth. The flux density on the rotor side is derived by equivalent magnetic circuit (EMC) with leakage magnetic flux. Taking the calculated flux density as one of the second boundary conditions, the air-gap field distribution is calculated by magnetic potential model with the eccentricity of the rotor. To verify the analytical method, we adopted the finite element method. The simulation results of the air-gap flux, back electromotive force, and cogging torque are in good agreement with the analytical results. Besides, applying the analytical model, the machine can be optimized for obtaining the optimal air-gap flux density distribution. The hybrid excitation machine with salient pole and interior magnets can provide a good flux density waveform. The study offers a helpful analytical method for design and optimization of the type of machine for ELVs.

INDEX TERMS Analytical method, hybrid excitation and interior permanent magnet machine, equivalent magnetic circuit (EMC), the eccentricity of the rotor.

I. INTRODUCTION

With the rapid development of e-commerce and express delivery, the challenges facing logistics vehicles are increasing [1], [2]. According to the European Commission, by 2030, the transportation of goods in central cities should produce no emissions at all. However, it accounts for 25% of urban carbon dioxide emissions, and the number of logistics vehicles is also increasing rapidly. A lot of research have been done on vehicle safety and comfort [3]–[6]. In the context of energy shortages and environmental degradation, the development of electric logistics vehicles (ELVs) is an effective solution to solve the problems and achieve sustainable development [7]–[9]. As the key component of the ELVs, hybrid excitation synchronous machines (HESMs) have the advantages of high power density of permanent magnet motor and controllable magnetic field of electric excitation motor, which can improve the efficiency of ELVs [10]–[12]. To improve the high efficiency of electric vehicles, the braking energy recovery and motor topology have always been the focus of many researchers [13]. Among various HESMs, parallel hybrid excitation synchronous machines (PHESMs) have some advantages over series hybrid excitation synchronous machines (SHESMs). The magnetic flux generated by the excitation windings does not pass through permanent magnets (PMs), reducing the magnetic resistance of the magnetic circuit and improving the machine efficiency [14]. The magnetomotive force (MMF) created by the armature windings forms a loop through the rotor core, avoiding the risk of PM demagnetization. By adjusting the excitation

The associate editor coordinating the review of this manuscript and approving it for publication was Zhiwu Li.

current, and changing the value of the synthetic magnetic field in the air-gap, the machine can operate under different working conditions [15]–[17].

The no-load air-gap magnetic field distribution is the basis of the design performance index of HESMs, such as back electric motive force (back-EMF), torque-speed and other performance. For design and optimization, the finite element method (FEM) and analytical method are often used to calculate the magnetic field [18]–[21]. However, no author has applied the analytical model to calculate the magnetic field of hybrid excitation and interior magnets machine considering the shape of stator and rotor teeth and the leakage magnetic flux. The FEM can analyze the magnetic field of various types of machines considering the effects of saturation and nonlinearity on the magnetic field distribution [22], [23], but it takes lots of time and computer source, its application in machine optimization and performance analysis is limited to some extent [24]–[26]. In [27], an analytical method for calculating the air-gap field distribution of SHESM is described in detail. It shows a structure in which two excitation sources are located in the rotor, each PM is placed on the surface of the salient pole. In [28], based on subdomain model, it presents an analytical method to predict of magnetic field distribution of parallel hybrid excitation and spoke-type tangential magnets motor with considering the tooth tips and shape of polar pieces. Each PM is placed on between two adjacent salient poles respectively. References [30], [31] provide other topologies of HESMs with complicated geometric structure, in which the studies are only done by the FEM.

The interior permanent magnets machines have the advantages of high power density and high efficiency, and have been widely used. Especially multisegment or multilayer interior magnets machines, which have additional reluctance torque, the torque density is higher. Due to the complicated magnetic flux path and leakage magnetic flux, the performance of these interior magnets machines is generally analyzed by the FEM [32]–[35], and few scholars use the analytical method [36]–[39]. To deal with the problem that the FEM needs a lot of computation time in the design process, an approach using the lumped equivalent magnetic circuit (EMC) method to calculate the electromagnetic performance of the interior magnets machine is proposed [36], [37]. In [38], the flux density of a multi-layered and multi-segmented interior permanent magnet machine is calculated by combining the EMC and conformal mapping with slotting effect. The EMC can only estimate the radial component of the flux density. According to the author's knowledge, there is no research on the hybrid analytical method for the interior permanent magnets machine that considers the shape of the stator and rotor teeth and the leakage magnetic flux. However, many scholars adopted the hybrid analysis method combining EMC and Maxwell's equations in the spoke-type magnets motor. To obtain the boundary condition on the rotor side, different models are presented considering the irregular PMs shape, teeth saturation, and the nonlinearity of magnetic materials, respectively [40]–[42].

This paper presents an analytical model of air-gap field in hybrid excitation and interior permanent magnets machine for ELVs, in which the shape of stator and rotor teeth is taken into account. The model combines the EMC and Maxwell's equations. To calculate the boundary conditions, the EMC models under different paths of hybrid excitation and interior permanent magnets machine and a specific calculation method for main permeance are given. The air-gap magnetic field is obtained by Maxwell's equations considering the rotor eccentricity. The model is verified by the FEM. Moreover, utilizing the analytical model, the machine is optimized by design the suitable pole-arc coefficients and the rotor eccentricity. In Section II, the topologies and features of the machine for ELVs are given. In Section III, the EMC model and calculation method for main permeance are derived, the model of the magnetic field distribution with the rotor eccentricity is established. In Section IV, the analytical model is verified, and the main structural parameters are optimized to improve the fundamental and reduce total harmonic distortion (THD) of the air-gap flux density. In Section V, the conclusions are summarized.

II. TOPOLOGY OF THE MACHINE

The configuration of the hybrid excitation and interior permanent magnets machine is shown in Fig. 1. In the machine, the rotor is composed of PM1 and PM2 which are built in the outer middle of the pole shoe and the excitation winding placed on the pole body in a series manner, which can increase the sine of air-gap flux density waveform. The magnetic flux of each pole is provided by the PM1, PM2, and excitation winding, the flux produced by the excitation winding does not pass through magnets, which can improve the motor efficiency and avoid demagnetization of PMs. The magnetic barrier is arranged to reduce the leakage magnetic flux. The magnetic bridge is set to connect the slots for PMs and pole shoes for the PMs. To simplify, assuming that the stator and rotor permeability is infinite. The eddy current, end and conductivity effects are neglected.

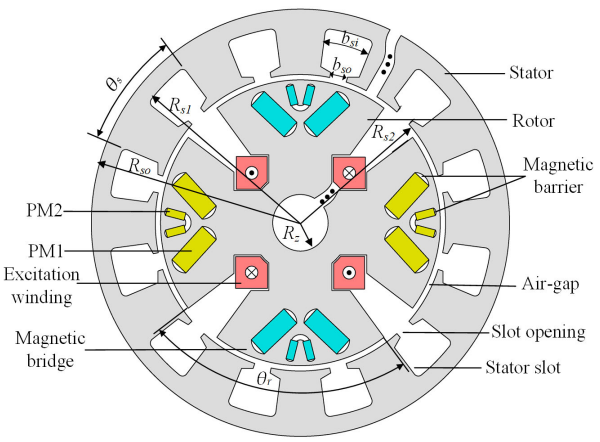

FIGURE 1. Structure of hybrid excitation and interior permanent magnets machine.

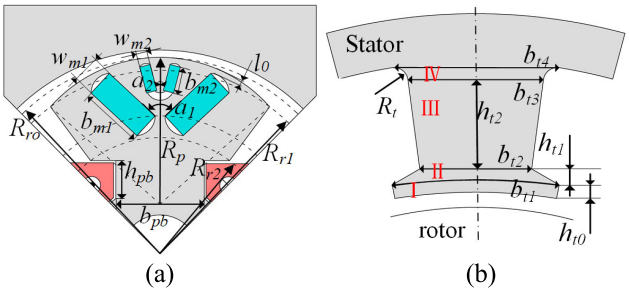

FIGURE 2. Partial structure of the machine (a) salient pole structure (b) stator tooth structure.

Partial structures of the machine including the salient pole and stator tooth are shown as Fig. 2. To improve the sine of the air-gap flux density waveform, the outer edge of the rotor core is designed as the non-circular shape, as shown in Fig. 2 (a). Due to the irregular structure of the stator tooth, the segmentation calculation is adopted, the segmentation diagram can be seen in Fig. 2 (b).

III. ANALYTICAL MODEL FOR THE MACHINE

Due to the complicated rotor topology of the hybrid excitation and interior permanent magnets machine shown in Fig. 1, the analytical calculation model of magnetic field for the machine is derived in detail. Firstly, the EMC model is established to derive the flux density on the rotor outer surface. Then, the radial and tangential of the air-gap flux density are calculated by considering the effect of the non-arc pole shoes. Finally, on the basis of the air-gap flux density, the expressions of cogging torque and back-EMF are given.

A. MAGNETIC CIRCUIT MODEL

Fig. 3 shows the magnetic line distribution of the machine in different states. It can be seen clearly that the flux of each

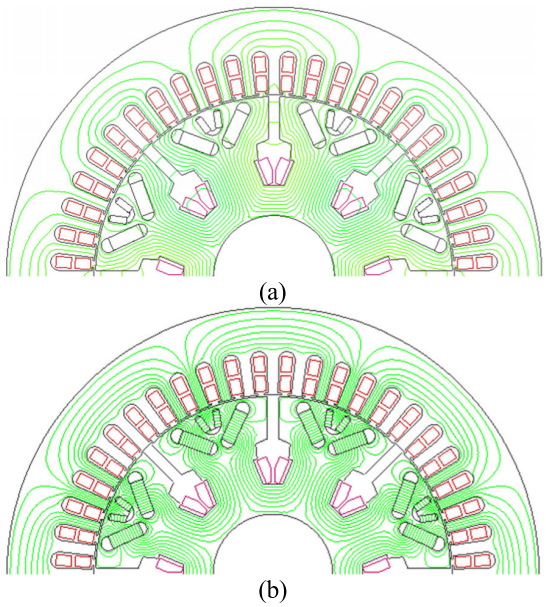

FIGURE 3. Distribution of magnetic flux in different states (a) flux by excitation winding alone (b) flux by PM1 and PM2.

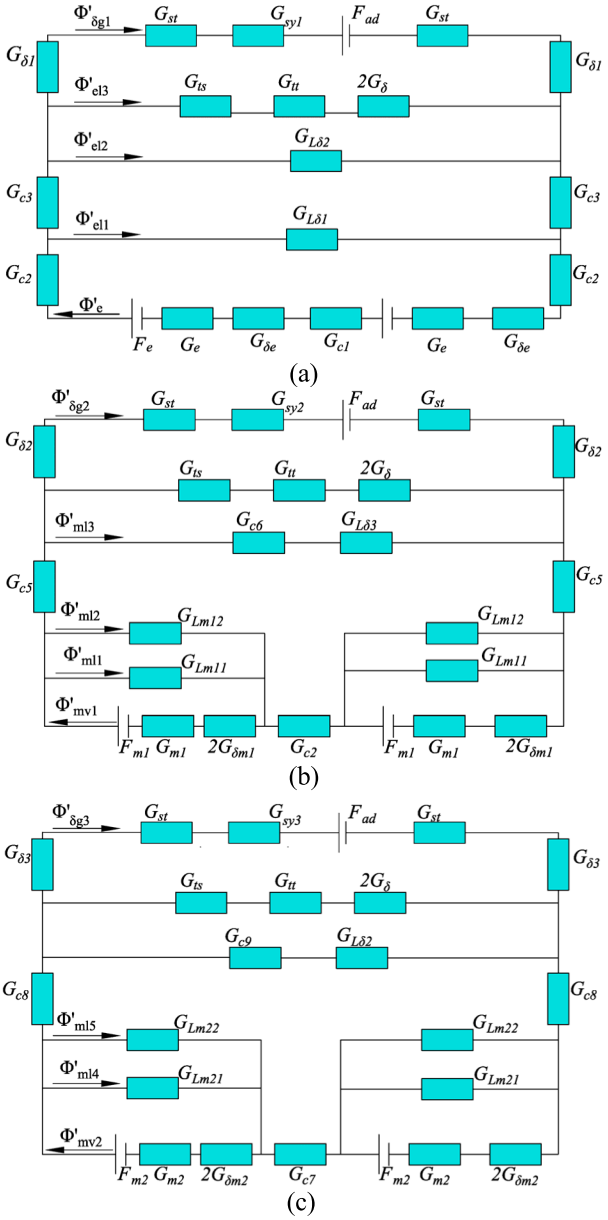

FIGURE 4. EMC model (a) magnetic flux path related to excitation winding (b) magnetic flux path related to PM1 (c) magnetic flux path related to PM2.

magnetic pole can be divided into two components, which are generated by the excitation winding and PM, respectively. Setting that the permeability of the PM is equal to that of vacuum, the magnetic flux generated alone by the excitation winding is obtained, as shown in Fig. 3 (a). The main magnetic flux is through the magnetic bridge of PM left and right to linkage armature winding. There are three leakage flux lines, including the leakage flux through the additional air gap between two adjacent pole shoes, and the additional air gap between two adjacent pole body, the stator teeth close to the air-gap. And setting the value of the excitation current is zero, the magnetic flux generated alone by the PM1 and PM2 are obtained, as shown in Fig. 3 (b). Fig. 3 (b) indicates

that the main magnetic flux created by PM1 and PM2 are both in series and in parallel. Similarly, there are three leakage flux lines, including the leakage flux through the magnetic bridge, the additional air gap between different poles, and the stator teeth close to air-gap.

As shown in Fig. 3, the studied machine has three magnetic potential sources on each pole, including electric excitation winding, PM1, and PM2. When the electric excitation source acts alone, the EMC diagram of electromagnetic can be obtained, as shown in Fig. 4 (a).

In a similar way, the EMC diagram of the other two magnetic potential sources under separate action can be obtained in Fig. 4 (b) and Fig. 4 (c).

Applying the superposition principle in electrotechnics, the total magnetic circuit for hybrid excitation and interior magnet machine can be obtained, as shown in Fig. 5. Due to the three magnetic potential sources occupy the different length of the salient pole, each pole shoe is divided into three parts, and the air-gap cross-sectional area can be regarded as three segments. Fig. 5 shows that the flux through the first part of the air-gap is provided only by the excitation winding, and the flux through the second part of the air-gap is provided by the excitation winding and PM1. At the same time, the flux through the third part of the air-gap is provided by the electric excitation winding, PM1, and PM2.

According to Fig. 5, the expression of the EMC model can be derived as follows by applying the Kirchhoff's law of magnetic circuits:

$$\begin{cases} \Phi_{ml4}+\Phi_{ml5}=\Phi_{mv2}-\Phi_{\delta g3} \\ \Phi_{ml1}+\Phi_{ml2}+\Phi_{\delta g2}-\Phi_{ml4}=\Phi_{mv1}-\Phi_{ml3} \\ \qquad -\Phi_{mv2}+\Phi_{ml5} \\ \Phi_{el1}+\Phi_{el2}+\Phi_{\delta g1}-\Phi_{ml1}-\Phi_{ml2}=\Phi_{e}-\Phi_{el3} \\ \qquad -\Phi_{mv1}+\Phi_{ml3} \end{cases} \tag{1}$$

$$\begin{cases} F_e-\Phi_e\dfrac{1}{2G_{zFe}}+\Phi_{el1}\dfrac{1}{2G_{ze1}}=0 \\ \Phi_{el3}\dfrac{1}{2G_{ze3}}-\Phi_{\delta g1}\left(\dfrac{1}{2G_{\delta 1}}+\dfrac{1}{G_{z\delta 1}}\right)=0 \\ 2F_{m1}-\Phi_{mv1}\dfrac{1}{2G_{zFm1}}-\Phi_{ml1}\dfrac{1}{2G_{Lml1}}=0 \\ \Phi_{ml3}\dfrac{1}{G_{zm3}}-\Phi_{\delta g2}\left(\dfrac{1}{2G_{\delta 2}}+\dfrac{1}{G_{z\delta 2}}\right) \\ \qquad +\Phi_{\delta g1}\left(\dfrac{1}{2G_{\delta 1}}+\dfrac{1}{G_{z\delta 1}}\right)=0 \\ 2F_{m2}-\Phi_{mv2}\dfrac{1}{2G_{zFm2}}-\Phi_{ml4}\dfrac{1}{2G_{Lm21}}=0 \\ \Phi_{ml5}\dfrac{1}{2G_{Lm22}}+\Phi_{\delta g2}\left(\dfrac{1}{2G_{\delta 2}}+\dfrac{1}{G_{z\delta 2}}\right) \\ \qquad -\Phi_{\delta g3}\left(\dfrac{1}{2G_{\delta 3}}+\dfrac{1}{G_{z\delta 3}}\right)=0 \end{cases} \tag{2}$$

F_e, F_{m1}, and F_{m2} are the MMF excited by excitation winding, PM1, and PM2 over one magnet pole, respectively, G_{m1} and G_{m2} are the magnetic permeance of PM1 and PM2, can be calculated by:

$$F_e = NI_f \tag{3}$$

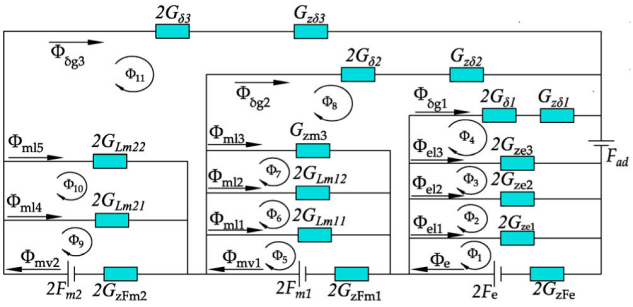

FIGURE 5. Total EMC model.

$$F_{m1} = H_r w_{m1} \tag{4}$$

$$F_{m2} = H_r w_{m2} \tag{5}$$

$$G_{m1} = \frac{1}{R_{m1}} = \frac{\mu_0\mu_m b_{m1} L_{ef}}{w_{m1}} \tag{6}$$

$$G_{m2} = \frac{1}{R_{m2}} = \frac{\mu_0\mu_m b_{m2} L_{ef}}{w_{m2}} \tag{7}$$

where N is the number of excitation winding turns, I_f is the excitation current, H_r is the intensity of the permanent magnetic field, μ_0 is the permeability of the vacuum, μ_m is the relative permeability of permanent magnet, w_{m1} and w_{m2} are the thickness of PM1 and PM2, b_{m1} and b_{m2} are the width of PM1 and PM2, L_{ef} is the effective length of the stator and rotor.

G_{Lm11} and G_{Lm12} are the leakage magnetic permeance of rotor core at top and bottom of PM1 over one magnet pole, G_{Lm21} and G_{Lm22} are the leakage magnetic permeance of rotor core at the top of PM2 and additional air gap at the bottom of PM2 over one magnet pole, respectively, $G_{L\delta 1}$ and $G_{L\delta 2}$ are the leakage magnetic permeance of the additional air gap between two adjacent pole shoes, can be calculated by:

$$G_{Lm11} = \frac{1}{R_{Lm11}} = \frac{\mu_0\mu_r L_{ef} l_0}{\pi l_0 - \frac{1}{2}w_{m1}} \tag{8}$$

$$G_{Lm12} = G_{Lm21} = \frac{1}{2}G_{Lm11} = \frac{1}{2R_{Lm11}} = \frac{1}{2}\frac{\mu_0\mu_r L_{ef} l_0}{\pi l_0 - \frac{1}{2}w_{m1}} \tag{9}$$

$$G_{Lm22} = \frac{1}{R_{Lm22}} = \frac{5\mu_0 L_{ef} l_0}{10w_{m2} - 6} \tag{10}$$

$$G_{L\delta 1} = G_{L\delta 2} = \mu_0\frac{8\left(R_{r1}-R_{r2}\right)L_{ef}}{\pi\left(R_{r1}+R_{r2}\right)\left(\theta_r-\alpha_{pe}\right)} \tag{11}$$

where μ_r is the relative permeability of the rotor core, R_{r1} and R_{r2} are the outer and inner radius of pole shoe, l_0 is the length of the magnetic bridge between the PM and the outer side of the rotor, α_{pe} is the pole-arc coefficient of the salient pole as shown in Fig. 6, θ_r are the rotor teeth pitch.

G_{tt} and G_{ts} are the tangential leakage magnetic permeance of stator tooth and slot, respectively, can be calculated by:

$$G_{tt} = \mu_0\mu_r\frac{2L_{ef}h_{t2}}{b_{t2}+b_{t3}} \tag{12}$$

$$G_{ts} = \mu_0\frac{L_{ef}h_{t0}}{b_{so}} \tag{13}$$

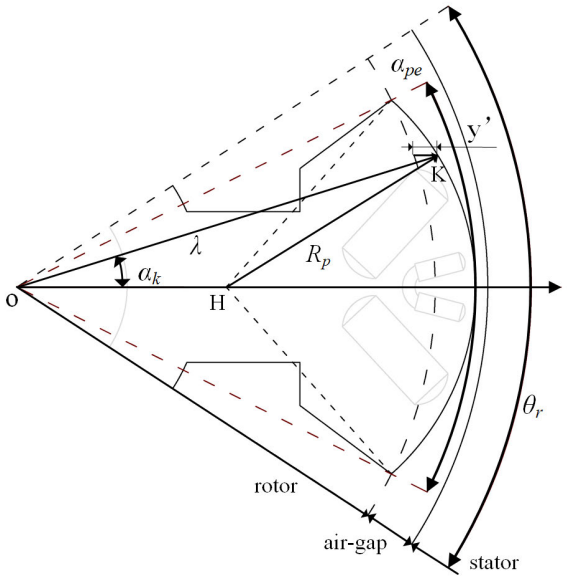

FIGURE 6. Geometric structure of the salient pole.

where h_{ti} and b_{ti} are the height and width of the ith region of the stator tooth, b_{so} are the width of slot opening.

$G_{\delta e}$, $G_{\delta m1}$, and $G_{\delta m2}$ are the magnetic permeance of the additional air gap between the rotor core and excitation winding, PM1, and PM2, respectively, $G_{\delta i}$ is the magnetic permeance of air-gap between the stator and rotor, can be calculated by:

$$G_{\delta e} = \mu_0 \frac{S_{\delta e}}{\delta_e} = \mu_0 \frac{2\left(b_{pb} + L_{ef}\right) h_{pb}}{\delta_e} \tag{14}$$

$$G_{\delta m1} = \mu_0 \frac{S_{m1}}{\delta_{m1}} = \mu_0 \frac{L_{ef} w_{m1}}{\delta_{m1}} \tag{15}$$

$$G_{\delta m2} = \mu_0 \frac{S_{m2}}{\delta_{m2}} = \mu_0 \frac{L_{ef} w_{m2}}{\delta_{m2}} \tag{16}$$

$$G_{\delta i} = \mu_0 \frac{S_\delta}{\delta_i} = \frac{\mu_0 \left(a_i - a_{i+1}\right) L_{ef} \pi}{2p\delta_i} \left(R_{s2} - \frac{1}{2}\delta_i\right) \tag{17}$$

where b_{pb} and h_{pb} are the width and height of pole body, δ_e, δ_{m1} and δ_{m2} are the additional air gap length between the rotor core and excitation winding, PM1, PM2. δ_i is the length of air-gap between the stator and rotor, a_i is the pole arc width in mechanical angle of the ith layer PMs.

G_{ci} is the magnetic permeance of the rotor core at the different position, can be calculated by:

$$G_{ci} = \frac{1}{R_{ci}} = \frac{l_c}{\mu_0 \mu_r S_c} \tag{18}$$

where S_c and l_c are the corresponding cross-sectional area and the length of the rotor core at different locations.

According to the segmentation method shown in Fig. 2(b), the stator tooth is treated as the superposition of four different areas, including an approximate rectangle (I), two trapezoids (II and III) and a quadrangle (IV). Due to the departments of I, II, III and IV are series connection, and the total permeance of stator tooth G_{st} can be calculated by:

$$\frac{1}{G_{st}} = \frac{1}{G_{st1}} + \frac{1}{G_{st2}} + \frac{1}{G_{st3}} + \frac{1}{G_{st4}} \tag{19}$$

① G_{st1} is the magnetic permeance in I region, and it can be calculated by:

$$G_{st1} = \mu_0 \mu_r L_{ef} \frac{b_{t1}}{h_{t1}} = \mu_0 \mu_r L_{ef} \frac{2\pi R_{s2}\theta_s - b_{so}}{h_{t0}} \tag{20}$$

where R_{s2} is the outer radius of stator core, θ_s is the stator teeth pitch.

② G_{st2} is the magnetic permeance in II region, and it can be calculated by:

$$G_{st2} = \mu_0 \mu_r L_{ef} \frac{2\pi R_{s2}\theta_s - b_{so} + b_{t2}}{2h_{t1}} \tag{21}$$

③ G_{st3} is the magnetic permeance in III region, and it can be calculated by:

$$G_{st3} = \mu_0 \mu_r L_{ef} \frac{b_{t2} + b_{t3}}{2h_{t2}} \tag{22}$$

④ G_{st4} is the magnetic permeance in IV region, and it can be calculated by:

$$\begin{aligned} G_{st4} &= \mu_0 \mu_r L_{ef} \frac{b_{t3} + b_{t4}}{2\left(R_{s1} - R_{s2} - \sum_{i=0}^{2} h_{ti}\right)} \\ &= \mu_0 \mu_r L_{ef} \frac{b_{t3} + 2\pi R_{so}\theta_s - 2R_t - b_{si}}{2\left(R_{s1} - R_{s2} - \sum_{i=0}^{2} h_{ti}\right)} \end{aligned} \tag{23}$$

where R_{so} is the outer radius of stator core, R_{s1} is the radius of stator slot bottom, R_t is the fillet radius in IV region.

G_{syi} is the stator yoke magnetic permeance, and it can be calculated by:

$$G_{\mathrm{syi}} = i\mu_0 \mu_r L_{ef} z \frac{\left(R_{so} - R_{s1}\right)}{\pi n_{st} \left(R_{so} + R_{s1}\right)} \tag{24}$$

where n_{st} is the amount of teeth across the stator.

The key permeability shown in Fig. 5 can be calculated by:

$$\begin{cases} G_{z\delta i} = 2G_{st} + G_{syi} \\ G_{zFx} = G_x + G_{\delta x} \\ G_{ze1} = G_{c2} + G_{L\delta 1} \\ G_{ze2} = G_{c2} + G_{c3} + G_{L\delta 2} \\ G_{ze3} = G_{c2} + G_{c3} + G_{tt} + G_{ts} + 2G_\delta \\ G_{zm3} = G_{c5} + G_{c6} + G_{L\delta 3} \end{cases} \tag{25}$$

Define A_{si} as the effective magnetic flux area corresponding to the ith magnetic potential source, so, when ψ represents the angle with reference to d axis, the flux density of outer side of the rotor and the Fourier expansion on the calculated position can be expressed as [40]:

$$B_{\delta \mathrm{i}} = \frac{\Phi_{\delta \mathrm{i}}}{A_{si}} \tag{26}$$

$$B_{pr\_out} = \sum_{\kappa=1}^{\infty} \frac{4}{\kappa\pi} B_{\delta \mathrm{i}} \sin\left(\frac{\kappa\pi\psi}{2}\right) \tag{27}$$

B. MAGNETIC FIELD DISTRIBUTION MODEL

Based on Maxwell's equations, the magnetic potential distribution $\Omega_{z\xi}$ can be expressed by the Laplace's equation:

$$\frac{\partial^2 \Omega_{z\xi}}{\partial r^2} + \frac{1}{r}\frac{\partial \Omega_{z\xi}}{\partial r} + \frac{1}{r^2}\frac{\partial^2 \Omega_{z\xi}}{\partial \alpha^2} = 0 \tag{28}$$

where r and α are the position of the calculated point, representing the radial length and the circumferential angle, respectively.

The general solution of (28) in different regions can be expressed by separation of variables method as follows:

$$\Omega_{zii} = \sum_m A_1 \left[\left(\frac{R_{s3}}{R_{s1}}\right)^{\frac{m\pi}{b_{si}}} \left(\frac{r}{R_{s1}}\right)^{\frac{m\pi}{b_{si}}} + \left(\frac{r}{R_{s3}}\right)^{-\frac{m\pi}{b_{si}}} \right] \times \cos\left[\frac{m\pi}{b_{si}}\left(\alpha + \frac{b_{si}}{2} - \alpha_i\right)\right] \tag{29}$$

$$\Omega_{ziii} = \sum_n A_2 \left[\left(\frac{r}{R_{s3}}\right)^{\frac{n\pi}{b_{so}}} + \left(\frac{r}{R_{s2}}\right)^{-\frac{m\pi}{b_{so}}} \right] \times \cos\left[\frac{m\pi}{b_{so}}\left(\alpha + \frac{b_{so}}{2} - \alpha_i\right)\right] \tag{30}$$

$$\Omega_{ziii} = \sum_k \left(A_3 \left(\frac{r}{R_{s2}}\right)^k + B_3 \left(\frac{r}{R_{ro}}\right)^{-k} \right) \cos(k\alpha) + \sum_k \left(C_3 \left(\frac{r}{R_{s2}}\right)^k + D_3 \left(\frac{r}{R_{ro}}\right)^{-k} \right) \sin(k\alpha) \tag{31}$$

where i, ii, and iii represent the regions of the slot, slot-opening, and air-gap. A1, A2, A3, B3, C3, and D3 are the coefficients to be determined. α_i is the angle of the ith slot, R_{ro} is the maximum radius of the rotor surface.

Under the same magnetic pole, the period of the flux density distribution is the same as that of the stator cogging. Equation (31) is simplified as:

$$\Omega_{ziii} = \sum_k \left(A_3 \left(\frac{r}{R_{s2}}\right)^k + B_3 \left(\frac{r}{R_{rO}}\right)^{-k} \right) \cos(k\alpha) \tag{32}$$

The boundary condition on the inside surface of the stator core can be calculated by:

$$B_\tau(r,\alpha)|_{r=R_{s2}} = 0 \tag{33}$$

If R_p is defined as the radius of the pole shoe surface, as shown in Fig. 6, the interfaces conditions on the outer surface of the pole shoe can be expressed by:

$$B_r(r,\alpha)|_{r=R_p} = -\mu_0 \frac{\partial \Omega_{ziii}}{\partial R_p} = B_{ps\_out} \tag{34}$$

where B_{ps_out} represents the average flux density on the pole shoe outer surface.

Combining (32) and (34), the radial magnetic flux density can be represented as:

$$B_r(r,\alpha) = -\mu_0 \frac{\partial \Omega_{ziii}}{\partial R_p}\frac{\partial R_p}{\partial r} = \frac{\partial R_p}{\partial r} \cdot B_{ps\_out} \tag{35}$$

Substituting (33) into (32), it can be obtained by:

$$B_3 = -A_3 \left(R_{s2}/R_{r0}\right)^k \tag{36}$$

Due to the salient pole structure of the machine, B_{ps_out} is equal to B_{pr_out}, the expression of interfaces conditions on the outer surface of the pole shoe by combining (32) and (35) can be derived and simplified by:

$$-\mu_0 \frac{k}{r}\left(A_3 \left(\frac{r}{R_{s2}}\right)^k - B_3 \left(\frac{r}{R_{r0}}\right)^{-k} \right) \cos(k\alpha) = \frac{4p}{k\pi} B_{\delta i} \sin\left(\frac{k\pi\psi}{2p}\right) \cdot \frac{\partial R_p}{\partial r} \tag{37}$$

In Fig. 6, h represents the eccentricity of the rotor, that is, the distance between the center of the rotor core and the salient pole, according to the geometric relationship in Fig. 6, h can be deduced by:

$$h = -\sqrt{R_p^2 - \left(R_{r1}\sin 2\pi\alpha_{pe}\right)^2} + R_{r1}\cos 2\pi\alpha_{pe} \tag{38}$$

Selecting the point K outside the salient pole randomly, and considering its coordinate as (x, y), it can be obtained by:

$$\lambda^2 - 2\lambda h\cos\alpha_k + h^2 - R_p^2 = 0 \tag{39}$$

where λ is the distance between the calculated point K and the origin, α_k is the angle between the line from point K to ordinate origin and the center axis of the salient pole.

Submitting (38) to (39), the expression of the radius of the pole shoe surface can be obtained by:

$$2\left(\lambda\cos\alpha_k - R_{r1}\cos\varphi\right)\sqrt{\left(R_p^2 - (R_{r1}\sin\varphi)^2\right)} = -\lambda^2 + 2\lambda R_{r1}\cos\varphi\cos\alpha_k - R_{r1}^2\left(2\cos^2\varphi - 1\right) \tag{40}$$

where φ is equal to $2\pi\alpha_{p1}$.

According to (40), the partial derivative of the radius of the pole shoe surface is calculated by:

$$\frac{\partial R_p}{\partial \lambda} = \cos\alpha_k\sqrt{\left(R_p^2 - (R_{r1}\sin\varphi)^2\right)} + \lambda - R_{r1}\cos\varphi\cos\alpha_k \tag{41}$$

Furthermore, the outside edge of the pole shoe is regarded as a parabola opening toward the origin of the coordinates, as shown in Fig. 6, the distance λ can be calculated by:

$$\lambda = R_{r1} + \Gamma\cos\alpha_k \tag{42}$$

In (42), Γ is the function expression of the proposed parabola, the variable Γ can be expressed by derivation and simplification:

$$\Gamma = -\left(\frac{256\lambda^2}{\pi^2 D^2 \alpha_{pe}^2}\cos^2\alpha_k - 1\right)(R_{r0} - R_{r1}) \tag{43}$$

Substituting (43) to (41), and it can be obtained by:

$$-\left(R_{r1} + (R_{ro} - R_{r1})\cos\alpha_k - \lambda\right)\pi^2 D^2 \alpha_{pe}^2 + 256\cos^3\alpha_k\left(R_{ro} - R_{r1}\right)\lambda^2 = 0 \tag{44}$$

Therefore, according to (36), (37) and (41), the coefficient A_3 can be obtained by:

$$A_3 = -4p\left(R_{r1}+\Gamma\right)\cos\alpha_k B_{\delta i}\sin\left(\frac{k\pi\psi}{2p}\right) \cdot \frac{\cos\alpha_k\sqrt{\left(R_p^2-(R_{r1}\sin\varphi)^2\right)}+R_{r1}(1-\cos\varphi\cos\alpha_k)+\Gamma}{\mu_0 k^2\pi\left(\left(R_{r1}+\Gamma\right)^k R_{s2}^{-k}+\left(R_{r1}+\Gamma\right)^{-k}R_{s2}^k\right)} \tag{45}$$

Based on (32), (38) and (44), the radial and circumferential of the air-gap flux density are calculated by:

$$B_r(r,\alpha) = 4p\cos^2\alpha_k B_{\delta i}\sin\left(\frac{k\pi\psi}{2p}\right) \cdot \frac{\sqrt{\left(R_p^2-(R_{r1}\sin\varphi)^2\right)}+R_{r1}(1-\cos\varphi\cos\alpha_k)+\Gamma}{rk\pi\left(\left(R_{r1}+\Gamma\right)^{k-1}R_{s2}^{-k}+\left(R_{r1}+\Gamma\right)^{-k-1}R_{s2}^k\right)} \cdot\sum_k\left(\left(\frac{r}{R_{s2}}\right)^k+\left(\frac{R_{s2}}{r}\right)^k\right)\cos k\left(\alpha-w_r t\right) \tag{46}$$

$$B_\tau(r,\alpha) = -4p\cos^2\alpha_k B_{\delta i}\sin\left(\frac{k\pi\psi}{2p}\right) \cdot \frac{\sqrt{\left(R_p^2-(R_{r1}\sin\varphi)^2\right)}+R_{r1}(1-\cos\varphi\cos\alpha_k)+\Gamma}{rk\pi\left(\left(R_{r1}+\Gamma\right)^{k-1}R_{s2}^{-k}+\left(R_{r1}+\Gamma\right)^{-k-1}R_{s2}^k\right)} \cdot\sum_k\left(\left(\frac{r}{R_{s2}}\right)^k-\left(\frac{R_{s2}}{r}\right)^k\right)\cos k\left(\alpha-w_r t\right) \tag{47}$$

Thus, combining (46), (47) with the Maxwell tensor method, by integration, cogging torque of the hybrid excitation machine is derived as:

$$T_{cog} = \frac{L_{ef}r^2}{\mu_0}\int_0^{2\pi} B_{r3}B_{\tau 3}d\alpha \tag{48}$$

The back-EMF of hybrid excitation machine is induced by the flux linkage in the winding which changes with time, it can be expressed as [17]:

$$E_\sigma = \frac{d\psi_\sigma}{dt} = \frac{d}{dt}\left(\frac{L_{ef}N_c}{a}\sum_{n\in\sigma}\left(\Omega_{z3}\big|_{\substack{r=R_s\\ \alpha=\alpha_{n+}}}-\Omega_{z3}\big|_{\substack{r=R_r\\ \alpha=\alpha_{n-}}}\right)\right) \tag{49}$$

where σ represents the phase A, B, and C of armature winding, a represents the number of parallel branches, N_c represents the turns per coil, α_n represents the angle of the slot where the coil is located.

The electromagnetic torque can be obtained by the principle of virtual displacement:

$$T_{em} = \frac{\sum\left(E_A I_A + E_B I_B + E_C I_C\right)}{w} \tag{50}$$

where w represents the rotor speed in rad/s, E_A, I_A, E_B, I_B, E_C, and I_C represent the back-EMFs and currents of phase A, B and C, respectively.

IV. FEA VALIDATION AND PERFORMANCE ANALYSIS

In this section, the calculated results of the radial and tangential of air-gap flux density, Back-EMF, and the cogging torque are compared with simulation results of that, the correctness of analytical model is verified. Based on the proposed analytical model, an optimization is performed to maximize the amplitude of the fundamental air-gap flux density and minimize THD of the air-gap flux density.

A. FEA VALIDATION

To verify the rationality and effectiveness of the analytical model, the 8-pole/48-slot hybrid excitation and interior permanent magnets machine is chosen as the simulation prototype. The main calculation and simulation parameters of the machine are listed in Table. 1. The parameters of the rotor are listed in Table. 2. The simulation model is established by the simulation software, in which all magnets is set as NdFeB. The stator and rotor adopt linear materials to approximate the infinite permeability in the assumptions in the simulation model. In the section, the simulation results and calculated results of the machine, including the air-gap flux, back-EMF and cogging torque are compared, respectively.

TABLE 1. Main parameters of the machines.

Symbol	Quantity	Value
m	The number of phase	3
p	The number of poles	4
Q	The number of stator slots	48
n_N	Rated speed	3000r/min
R_{so}	Radius of the stator outer surface	80mm
R_{sl}	Radius of the slot bottom	73mm
R_{s2}	Radius of the stator inner surface	53.5mm
R_z	Radius of the shaft	18mm
δ_{mi}	Length of the air-gap	0.5mm

TABLE 2. The parameters of the rotor.

Symbol	Quantity	Value
b_{mv1}	The width of PM1	12mm
w_{mv1}	The thickness of PM1	4mm
b_{mv2}	The width of PM2	5mm
w_{mv2}	The thickness of PM2	2mm
R_{ro}	Maximum radius of the rotor surface	53mm
R_{r1}	Outer radius of the pole shoe	52mm
R_{r2}	Inner radius of the pole shoe	39mm
θ_r	Rotor teeth pitch	0.87rad

The air-gap flux density of the hybrid excitation and interior permanent magnets machine is drawn in Fig. 7. Selecting the center position of the air-gap, the radial and tangential component of the air-gap field are calculated. It can be seen that for the eccentric salient pole structure of the hybrid excitation and interior permanent magnets machine, the curve of the analytical results and that of the simulation results have

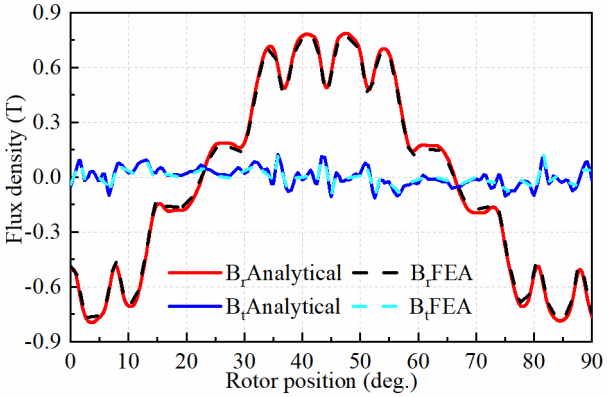

FIGURE 7. Air-gap flux density curve of the studied machine.

a high degree of agreement, which shows that the analytical model can calculate the radial and tangential of air-gap flux density. In addition, the analytical results in the stator slot and the salient pole are similar to the simulation results, indicating that the analysis model can consider the influence of the shape of the stator and rotor teeth on the air-gap flux density. It is worth noting that the sine of the air-gap flux density waveform is relatively high.

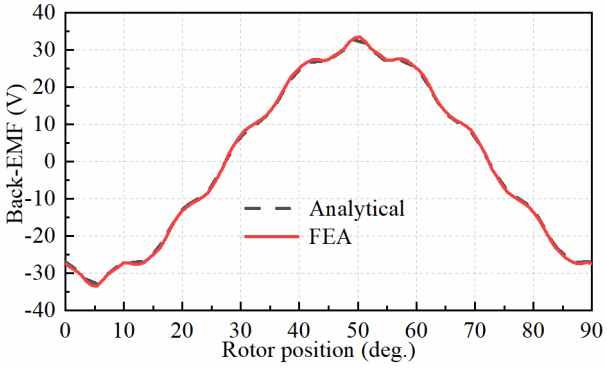

FIGURE 8. Back-EMF curves of the studied machine.

Fig. 8 shows that the Back-EMF curves of single phase under no-load condition. The simulation curve of the Back-EMF is very close to the calculation curve of that, which proves the analytical model can be used to obtain the Back-EMF of the studied machine under no-load condition. Besides, the curves shown in Fig. 8 are close to the sinusoidal waveform, which indicates that the structure of the provided salient pole rotor can enhance the output quality of the machine.

Fig. 9 shows that cogging torque curves obtained by analytical calculation and simulation, respectively. It can be seen that the cogging torque waveform predicted by the analytical model has a small difference with the simulation result, which further proves the feasibility and practicability of the analytical method. Due to the analytical model of magnetic field proposed in this paper takes into account the influence of stator slotting and the non-circular outer edge of the rotor,

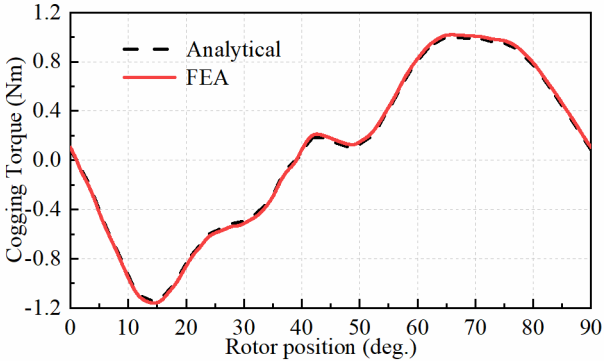

FIGURE 9. Cogging torque of the studied machine.

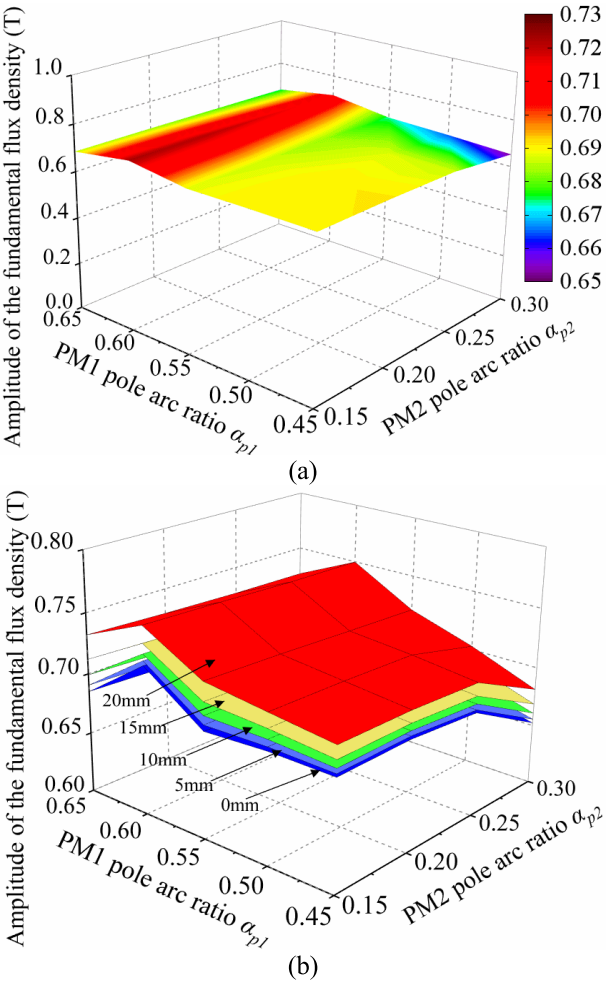

FIGURE 10. The amplitude of the fundamental air-gap flux density. (a) $h = 0$, (b) with different eccentricity h.

the cogging torque model obtained by the calculation method is also affected by the cogging effect.

Table. 3 shows the comparisons of the root mean square (RMS) of radial and tangential air-gap flux density, back-EMF and cogging torque of the machine. It can be seen that using the analytical model and FEA, the RMS of radial air-gap flux density of the machine is about 0.5 T, and the cogging torque is about 500 mNm, the back-EMF

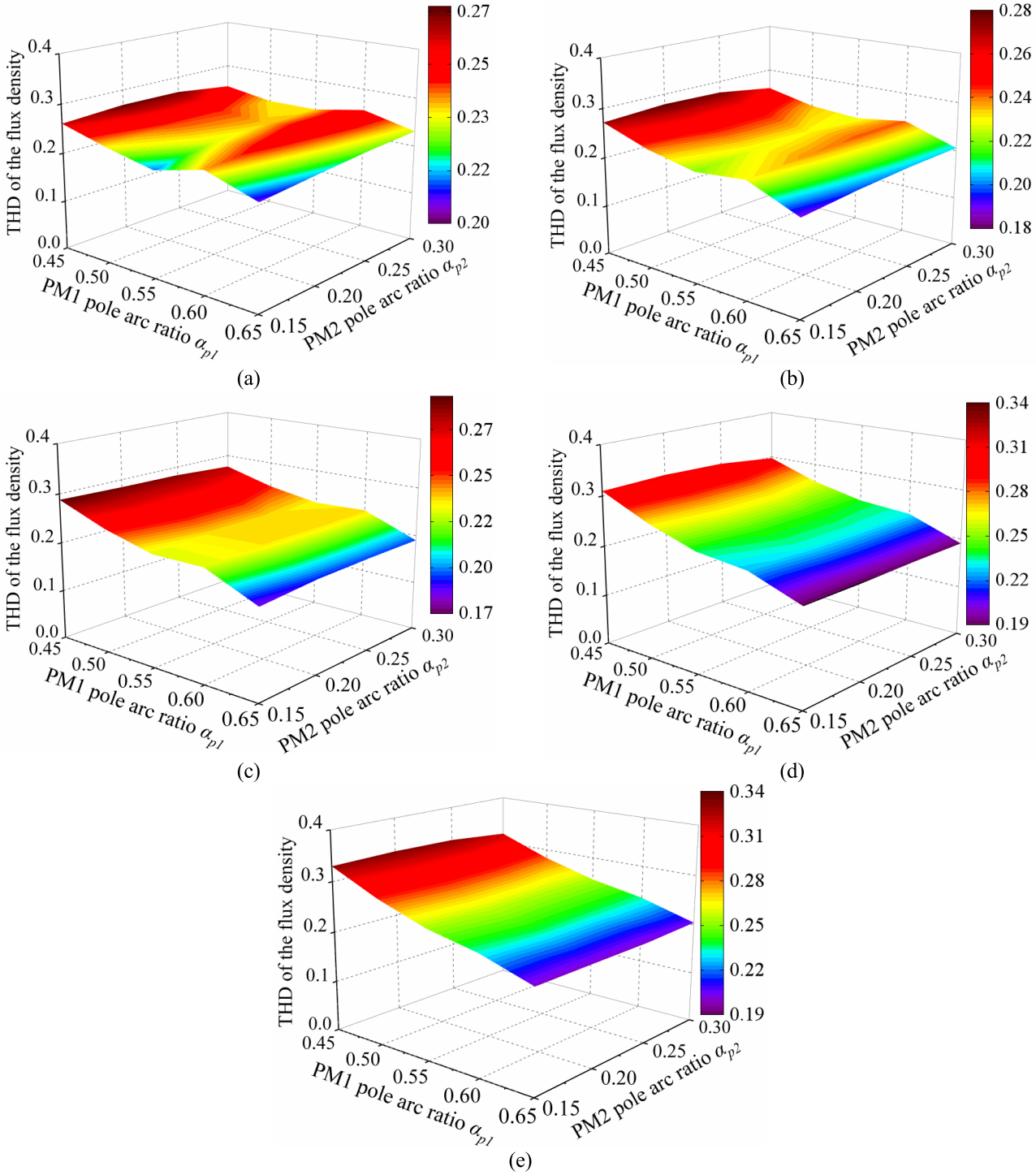

FIGURE 11. THD of air-gap flux density with different eccentricity *h*. (a) $h = 0$, (b) $h = 5$, (c) $h = 10$, (d) $h = 15$, (e) $h = 20$.

is about 21 V, which indicates that the RMS of calculated by the analytical model are close to those of FEA.

B. PERFORMANCE ANALYSIS

The pole-arc coefficient corresponding to each excitation source of a single magnetic pole is a crucial factor affecting the amplitude of the fundamental of air-gap field and the distribution of the harmonic of air-gap field. Due to the space of pole shoe of the studied machine is limited, in order to maximize the electromagnet field utilization, the pole-arc coefficient of the pole shoe through the electric excitation source α_{pe} is selected as 0.91. Moreover, the non-circular

TABLE 3. The comparisons of RMS.

	Radial flux density (T)	Tangential flux density (mT)	Back-EMF(V)	Cogging torque (Nm)
FEA	0.501	1.402	21.081	0.465
Analytical	0.519	2.069	21.946	0.441

structure of the rotor surface is adopted in the machine. It is quite obvious that the eccentricity is also a crucial factor which can affect the distribution of air-gap field. h is defined as the eccentricity of the rotor, α_{p1} and α_{p2} are defined as the pole-arc coefficients of the PM1 and PM2. Therefore, the influence of the arrangement form of the pole shoe and PM1, PM2 is researched by using the proposed analytical model, that is, the different combination of h, α_{p1} and α_{p2} are analyzed for the optimum distribution of air-gap field, as shown in Fig. 10-12.

Fig. 10 shows the amplitude of the fundamental air-gap flux density under the different eccentricity. In Fig. 10 (a), it can be seen clearly that when α_{pe} remains unchanged, the fundamental amplitude of the air-gap flux density enhances as α_{p1} and α_{p2} increase, which is caused by the increase in volume of PMs. Besides, compared with α_{p2}, α_{p1} has a greater influence on the fundamental of air-gap flux density. Further, it can be seen that compared with α_{p1} and α_{p2}, the eccentricity has the greatest effect on the fundamental amplitude of the air-gap flux density, as shown in Fig. 10 (b). When h is set to 0, 5, 10, 15, and 20, respectively, the fundamental amplitude of the air-gap flux density increases slowly at first, and then more quickly.

Keeping α_{pe} constant and changing α_{p1}, α_{p2}, and h, the variation of THD of the air-gap flux density will be more complicated. Therefore, The THD with different eccentricity h is analyzed, in which the pole-arc coefficients of PM1 and PM2 are set within a standard range, it is because of the need to ensure the maximization of the sine flux waveform. From Fig. 11, we can see that h has the most significant influence on the THD, whereas α_{p2} has the least influence on the THD. Furthermore, with the increasing of h, the THD decreases at first and then increases gradually. When h is from 0 to 10, THD decreases, the minimum value of THD decreases from 0.2 to 0.17. When h is from 10 to 15, THD increases, the minimum and maximum of THD increases from 0.17 to 0.19, and from 0.29 to 0.34, respectively, but the increasing of the THD is smaller. When h is from 15 to 20, THD still increases, however, compared with the previous one, the scope of the increase is bigger. Besides, All the THD with different eccentricity shown in Fig. 11 is less than 0.3. When h is 10 or 15, the area with the THD below 20% is the largest, which can be seen in Fig. 11 (c) and Fig. 11 (d). When h is 20, the area with the THD above 31% is the widest, which can be seen in Fig. 11 (e).

By combining Fig. 10 (b) and Fig. 11 (e), it is obvious that with the increasing of h, the fundamental air-gap flux density always keeps increasing, but when h exceeds a certain value,

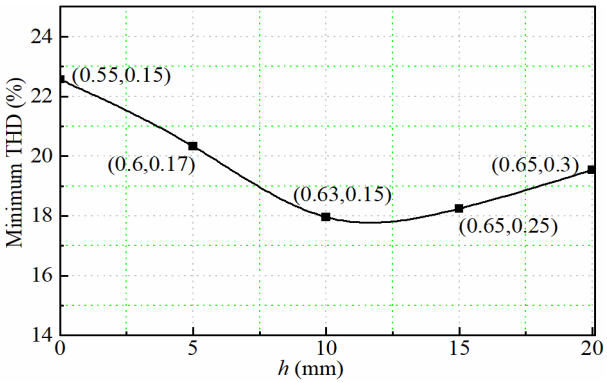

FIGURE 12. Minimum THD distribution with different eccentricity *h*.

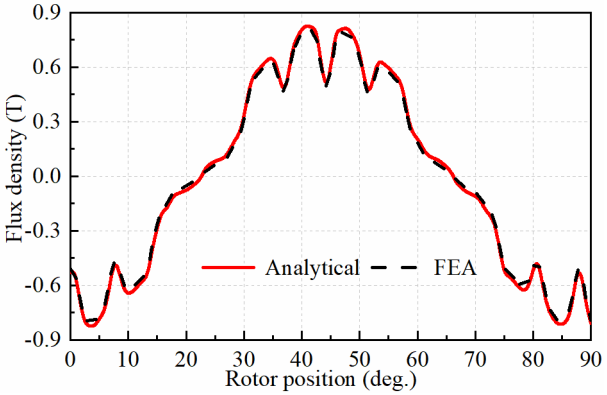

FIGURE 13. Air-gap flux density curve of the optimized machine.

the THD also increases. Therefore, both the fundamental and THD of air-gap flux density should be taken into account to design the eccentricity of the rotor. Aiming at the minimum THD, the optimal parameters h, α_{p1}, and α_{p2} can be obtained. The optimal combination of α_{p1} and α_{p2} with different h is given, as shown in Fig. 12. Similar to the results obtained in Fig. 11, when h is from 10 to 15, the THD is the smallest. α_{p1} and α_{p2} are 0.65 and 0.25, respectively, and h is 15, minimum THD is obtained. When the eccentricity of the rotor, the pole-arc coefficients of the PM1and PM2 are 15, 0.65 and 0.25, the radial air-gap flux density distribution is given, as shown in Fig.13. Comparing with the initial radial air-gap flux density curve in Fig.7, the air-gap flux density waveform of the optimized machine is closer to a sine curve, and the analytical result is in good agreement with the simulation result.

V. CONCLUSION

In this paper, aiming at the magnetic field analysis of the hybrid excitation and interior permanent magnets machine for ELVs, the analytical method is proposed for predicting the air-gap field distribution. In the analytical model, the EMC method and magnetic potential analysis method are combined, and the shape of the stator and rotor teeth is considered. To obtain the boundary conditions, the EMC

model considering the stator teeth shape and the leakage flux is established for calculating the air-gap flux density on the rotor side, which can also provide theoretical foundation for reducing the magnetic leakage. Applying Maxwell's equation, the magnetic field model is obtained by accounting for the eccentricity of the rotor.

The analytical method is verified by using the simulation model. The result shows that the analytical model can be adopted to calculate the electromagnetic performance of this type of machine, including the air-gap field, back-EMF and cogging torque. By utilizing the analytical model, the pole-arc coefficients of PM1, PM2, and the rotor eccentricity are optimized to get maximum fundamental and minimum THD of air-gap flux density. Moreover, compared with the former, the eccentricity has a greater influence on the air-gap field distribution of the studied machine. For the hybrid excitation and interior permanent magnets machine, under the condition of ensuring the maximization of electromagnetic utilization, the distribution of the air-gap field can be improved by changing the pole-arc coefficients of PM1 and the rotor eccentricity, thus improving the operational quality of the machine. In addition, the machine can improve the quality of the air-gap flux waveform to make the THD of that below 30%.

There is still much work to be done on the analytical modeling of the hybrid excitation and interior permanent magnets machine for ELVs. In the future work, the application of the method to other machines of this type will be involved. In order to get more precise results, it is necessary to consider the nonlinear characteristics of the materials of stator and rotor in the machine. In addition, the efficiency and control strategy of the machine should also be further studied.

FREQUENTLY USED SYMBOLS

N	Number of excitation winding turns
I_f	Excitation current
H_r	Intensity of the permanent magnetic field
μ_0	Permeability of the vacuum
μ_m	Relative permeability of permanent magnet
w_{m1}	Thickness of PM1
w_{m2}	Thickness of PM2
b_{m1}	Width of PM1
b_{m2}	Width of PM2
L_{ef}	Effective length of the stator and rotor
μ_r	Relative permeability of the rotor core
R_{r1}	Outer radius of pole shoe
R_{r2}	Inner radius of pole shoe
l_0	Length of the magnetic bridge between the PM and the outer side of the rotor
α_{pe}	Pole-arc coefficient of the salient pole
h_{ti}	Height of the ith region of the stator tooth
b_{ti}	Width of the ith region of the stator tooth
b_{pb}	Width of pole body
h_{pb}	Height of pole body
δ_e	Additional air gap length between the rotor core and excitation winding
δ_{m1}	Additional air gap length between the rotor core and PM1
δ_{m2}	Additional air gap length between the rotor core and PM2
R_p	Radius of the pole shoe surface
h	Eccentricity of the rotor
λ	Distance between the calculated point and the origin
α_k	Angle between the line from point to ordinate origin and the center axis of the salient pole

REFERENCES

[1] W. Wang, G. Tian, M. Chen, F. Tao, C. Zhang, A. Ai-Ahmari, Z. Li, and Z. Jiang, "Dual-objective program and improved artificial bee colony for the optimization of energy-conscious milling parameters subject to multiple constraints," *J. Cleaner Prod.*, vol. 245, Feb. 2020, Art. no. 118714.

[2] G. Tian, H. Zhang, Y. Feng, H. Jia, C. Zhang, Z. Jiang, Z. Li, and P. Li, "Operation patterns analysis of automotive components remanufacturing industry development in China," *J. Cleaner Prod.*, vol. 164, pp. 1363–1375, Oct. 2017.

[3] X. Sun, H. Zhang, W. Meng, R. Zhang, K. Li, and T. Peng, "Primary resonance analysis and vibration suppression for the harmonically excited nonlinear suspension system using a pair of symmetric viscoelastic buffers," *Nonlinear Dyn.*, vol. 94, no. 2, pp. 1243–1265, Oct. 2018, doi: 10.1007/s11071-018-4421-9.

[4] H. Zhang, Y. Peng, L. Hou, D. Wang, G. Tian, and Z. Li, "Multistage impact energy distribution for whole vehicles in high-speed train collisions: Modeling and solution methodology," *IEEE Trans. Ind. Informat.*, vol. 16, no. 4, pp. 2486–2499, Apr. 2020.

[5] H. Zhang, Y. Peng, L. Hou, G. Tian, and Z. Li, "A hybrid multi-objective optimization approach for energy-absorbing structures in train collisions," *Inf. Sci.*, vol. 481, pp. 491–506, May 2019.

[6] R.-H. Zhang, Z.-C. He, H.-W. Wang, F. You, and K.-N. Li, "Study on self-tuning tyre friction control for developing main-servo loop integrated chassis control system," *IEEE Access*, vol. 5, pp. 6649–6660, 2017.

[7] Z. Zhao, T. Wang, J. Shi, B. Zhang, R. Zhang, M. Li, and Y. Wen, "Analysis and application of the piezoelectric energy harvester on light electric logistics vehicle suspension systems," *Energy Sci. Eng.*, vol. 7, no. 6, pp. 2741–2755, Dec. 2019.

[8] P. Lebeau, C. Macharis, and J. Van Mierlo, "Exploring the choice of battery electric vehicles in city logistics: A conjoint-based choice analysis," *Transp. Res. E, Logistics Transp. Rev.*, vol. 91, pp. 245–258, Jul. 2016.

[9] Y. Li, M. K. Lim, Y. Tan, S. Y. Lee, and M.-L. Tseng, "Sharing economy to improve routing for urban logistics distribution using electric vehicles," *Resour., Conservation Recycling*, vol. 153, Feb. 2020, Art. no. 104585.

[10] Y. Liu, Z. Zhang, and X. Zhang, "Design and optimization of hybrid excitation synchronous machines with magnetic shunting rotor for electric vehicle traction applications," *IEEE Trans. Ind. Appl.*, vol. 53, no. 6, pp. 5252–5261, Nov. 2017.

[11] Z. Zhang, S. Ma, J. Dai, and Y. Yan, "Investigation of hybrid excitation synchronous machines with axial auxiliary air-gaps and nonuniform air-gaps," *IEEE Trans. Ind. Appl.*, vol. 50, no. 3, pp. 1729–1737, May 2014.

[12] H. Hua and Z. Q. Zhu, "Novel parallel hybrid excited machines with separate stators," *IEEE Trans. Energy Convers.*, vol. 31, no. 3, pp. 1212–1220, Sep. 2016.

[13] H. Xiong, X. Zhu, and R. Zhang, "Energy recovery strategy numerical simulation for dual axle drive pure electric vehicle based on motor loss model and big data calculation," *Complexity*, vol. 2018, Aug. 2018, Art. no. 4071743, doi: 10.1155/2018/4071743.

[14] W. Hu, X. Zhang, H. Yin, H. Geng, Y. Zhang, and L. Shi, "Analysis of magnetic field and electromagnetic performance of a new hybrid excitation synchronous motor with dual-V type magnets," *Energies*, vol. 13, no. 6, p. 1501, Mar. 2020.

[15] G. Zhang, W. Hua, M. Cheng, and J. Liao, "Design and comparison of two six-phase hybrid-excited flux-switching machines for EV/HEV applications," *IEEE Trans. Ind. Electron.*, vol. 63, no. 1, pp. 481–493, Jan. 2016.

[16] J. A. Tapia, F. Leonardi, and T. A. Lipo, "Consequent-pole permanent-magnet machine with extended field-weakening capability," *IEEE Trans. Ind. Appl.*, vol. 39, no. 6, pp. 1704–1709, Nov. 2003.

[17] W. Ding, S. Yang, and Y. Hu, "Development and investigation on segmented-stator hybrid-excitation switched reluctance machines with different rotor pole numbers," *IEEE Trans. Ind. Electron.*, vol. 65, no. 5, pp. 3784–3794, May 2018.
[18] S. S. Maroufian and P. Pillay, "Torque characterization of a synchronous reluctance machine using an analytical model," *IEEE Trans. Transport. Electrific.*, vol. 4, no. 2, pp. 506–516, Jun. 2018.
[19] B. Guo, Y. Huang, F. Peng, and J. Dong, "General analytical modeling for magnet demagnetization in surface mounted permanent magnet machines," *IEEE Trans. Ind. Electron.*, vol. 66, no. 8, pp. 5830–5838, Aug. 2019.
[20] Y. Oner, Z. Q. Zhu, L. J. Wu, X. Ge, H. Zhan, and J. T. Chen, "Analytical on-load subdomain field model of permanent-magnet Vernier machines," *IEEE Trans. Ind. Electron.*, vol. 63, no. 7, pp. 4105–4117, Jul. 2016.
[21] S. G. Min, G. Bramerdorfer, and B. Sarlioglu, "Analytical modeling and optimization for electromagnetic performances of fractional-slot PM brushless machines," *IEEE Trans. Ind. Electron.*, vol. 65, no. 5, pp. 4017–4027, May 2018.
[22] J. H. Seo and H. S. Choi, "Analytical modeling for calculating cogging torque in interior permanent magnet machine with multi flux-barriers," *IEEE Trans. Appl. Supercond.*, vol. 24, no. 3, pp. 1–4, Jun. 2014.
[23] A. A. Diriye, S. Ouagued, Y. Amara, and G. Barakat, "Performance analysis of a series hybrid excited synchronous machine by a hybrid analytical model," in *Proc. 10th Int. Conf. Ecological Vehicles Renew. Energies (EVER)*, Monte Carlo, Monaco, Mar. 2015, pp. 1–6.
[24] Z. Zhang, C. Xia, Y. Yan, Q. Geng, and T. Shi, "A hybrid analytical model for open-circuit field calculation of multilayer interior permanent magnet machines," *J. Magn. Magn. Mater.*, vol. 435, pp. 136–145, Aug. 2017.
[25] W. Kemmetmüller, D. Faustner, and A. Kugi, "Modeling of a permanent magnet synchronous machine with internal magnets using magnetic equivalent circuits," *IEEE Trans. Magn.*, vol. 50, no. 6, pp. 1–14, Jun. 2014.
[26] C. Xia, Z. Zhang, and Q. Geng, "Analytical modeling and analysis of surface mounted permanent magnet machines with skewed slots," *IEEE Trans. Magn.*, vol. 51, no. 5, pp. 1–8, May 2015.
[27] H. Bali, Y. Amara, G. Barakat, R. Ibtiouen, and M. Gabsi, "Analytical modeling of open circuit magnetic field in wound field and series double excitation synchronous machines," *IEEE Trans. Magn.*, vol. 46, no. 10, pp. 3802–3815, Oct. 2010.
[28] K. Boughrara, R. Ibtiouen, and T. Lubin, "Analytical prediction of magnetic field in parallel double excitation and spoke-type permanent-magnet machines accounting for tooth-tips and shape of polar pieces," *IEEE Trans. Magn.*, vol. 48, no. 7, pp. 2121–2137, Jul. 2012.
[29] Y. Liu, Z. Zhang, C. Wang, and H. Gao, "Optimization and performance improvement of a hybrid excitation synchronous machine with modular magnetic-shunting rotor," *IEEE Trans. Ind. Electron.*, vol. 67, no. 6, pp. 4381–4390, Jun. 2020.
[30] Y. Liu, Z. Zhang, C. Wang, W. Geng, and H. Wang, "Electromagnetic performance analysis of a new hybrid excitation synchronous machine for electric vehicle applications," *IEEE Trans. Magn.*, vol. 54, no. 11, pp. 1–4, Nov. 2018.
[31] D. Xu, M. Y. Lin, and X. H. Fu, "Design and analysis of a hybrid axial field flux-switching permanent magnet machine," in *Proc. ASEMD*, Shanghai, China, 2015, pp. 314–315.
[32] F. Chai, Y. Li, Y. Pei, and Y. Yu, "Analysis of radial vibration caused by magnetic force and torque pulsation in interior permanent magnet synchronous motors considering air-gap deformations," *IEEE Trans. Ind. Electron.*, vol. 66, no. 9, pp. 6703–6714, Sep. 2019.
[33] M. S. Shin, K.-H. Shin, J.-Y. Choi, and H.-W. Cho, "Random optimization method to reduce cogging torque of interior permanent magnet synchronous motor," *J. Magn.*, vol. 24, no. 4, pp. 577–582, Dec. 2019.
[34] H. I. Park, S. Kyung-Hun, Y. Hyun-Sup, and C. Jang-Young, "Design and characteristic analysis for high-speed interior permanent magnet synchronous motor with ferrite magnet," *Trans. Korean Inst. Electr. Eng.*, vol. 65, no. 11, pp. 12–1806, Nov. 2016.
[35] S. Okamoto, N. Denis, Y. Kato, M. Ieki, and K. Fujisaki, "Core loss reduction of an interior permanent-magnet synchronous motor using amorphous stator core," *IEEE Trans. Ind. Appl.*, vol. 52, no. 3, pp. 2261–2268, May 2016.
[36] J.-G. Lee, D.-K. Lim, and H.-K. Jung, "Analysis and design of interior permanent magnet synchronous motor using a sequential-stage magnetic equivalent circuit," *IEEE Trans. Magn.*, vol. 55, no. 10, pp. 1–4, Oct. 2019.
[37] L. Zhu, S. Z. Jiang, Z. Q. Zhu, and C. C. Chan, "Analytical modeling of open-circuit air-gap field distributions in multisegment and multilayer interior permanent-magnet machines," *IEEE Trans. Magn.*, vol. 45, no. 8, pp. 3121–3130, Aug. 2009.
[38] D.-K. Lim, K.-P. Yi, D.-K. Woo, H.-K. Yeo, J.-S. Ro, C.-G. Lee, and H.-K. Jung, "Analysis and design of a multi-layered and multi-segmented interior permanent magnet motor by using an analytic method," *IEEE Trans. Magn.*, vol. 50, no. 6, pp. 1–8, Jun. 2014.
[39] X. Zhang, Q. Du, S. Ma, H. Geng, W. Hu, Z. Li, and G. Liu, "Permeance analysis and calculation of the double-radial rare-Earth permanent magnet voltage-stabilizing generation device," *IEEE Access*, vol. 6, pp. 23939–23947, 2018.
[40] Y.-X. Liu, L.-Y. Li, Q.-H. Gao, J.-W. Cao, R.-H. Wang, and Z.-Y. Sun, "Analytical model of torque-prediction for a novel hybrid rotor permanent magnet machines," *IEEE Access*, vol. 7, pp. 109528–109538, 2019.
[41] P. Liang, F. Chai, Y. Yu, and L. Chen, "Analytical model of a spoke-type permanent magnet synchronous in-wheel motor with trapezoid magnet accounting for tooth saturation," *IEEE Trans. Ind. Electron.*, vol. 66, no. 2, pp. 1162–1171, Feb. 2019.
[42] P. Liang, F. Chai, Y. Bi, Y. Pei, and S. Cheng, "Analytical model and design of spoke-type permanent-magnet machines accounting for saturation and nonlinearity of magnetic bridges," *J. Magn. Magn. Mater.*, vol. 417, no. 2, pp. 389–396, Nov. 2016.

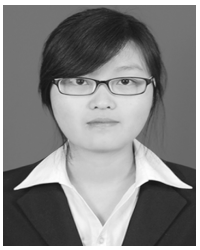

WENJING HU received the B.S. and M.S. degrees in vehicle engineering from the Shandong University of Technology, Zibo, China, in 2015 and 2017, respectively, where she is currently pursuing the Ph.D. degree with the Transportation and Vehicle Engineering School.

Her research interests include vehicle engineering, automotive electronics, design and manufacture of motor, and new energy electric vehicle technology.

XUEYI ZHANG received the M.S. degree in mechanical manufacturing automation from Guangxi University, Guangxi, China, in 1990, and the Ph.D. degree in mechanical and electronic engineering from the Shandong University of Science and Technology, Qingdao, China, in 2011. He is currently working on research and development of vehicle's motor and electric vehicles with the Transportation and Vehicle Engineering School, Shandong University of Technology. He is also a National Candidate with the Millions of Talents. He enjoys the State Department Special Allowance. He holds 21 authorized patents. He has released 112 articles and published five monographs. He received the Second Award of the National Technical Invention and six items of the second prizes at provincial and ministerial level.

YULONG LEI received the Ph.D. degree in vehicle engineering from the Jilin University of Technology, Changchun, China, in 1999, and the Ph.D. degree in transportation engineering from Jilin University, Changchun, in 2002. He is currently working on research of automobile transmission system theory and control technology with the College of Automotive Engineering, Jilin University. He has completed 23 national and provincial scientific research projects. He holds over 43 authorized patents. He has released 165 articles. He was selected from the New Century Talent Program, Ministry of Education. He received the Excellent Science and Technology Talent Award of China Automobile Industry, the First Prize of the Science and Technology Progress of Jilin Province, and the First Prize of the Science and Technology Invention, Chinese Association of Automation.

QINJUN DU received the M.S. degree in agricultural electrical and automation from China Agricultural University, Beijing, China, in 2003, and the Ph.D. degree in bionic technology from the Beijing Institute of Technology, Beijing, China, in 2007. He is currently working on research and development of electronic and electrical technology for vehicle with the School of Electrical and Electronic Engineering, Shandong University of Technology. He has released 46 articles. He received the Young Experts with Outstanding Contributions, Shandong, the Second Award of the National Technical Invention, and three items of the second prize at provincial and ministerial level.

LIWEI SHI received the M.S. degree in vehicle engineering from the Shandong University of Technology (SUT), Zibo, China, in 2005, and the Ph.D. degree in electrical engineering and automation from the Nanjing University of Aeronautics and Astronautics, Nanjing, China, in 2017.

He is currently working on research and development of vehicle's motors and electric vehicles with the Transportation and Vehicle Engineering School, SUT. He holds 32 authorized patents. He has published 22 articles and two monographs. He was a recipient of the Second Award of National Technical Invention and five items of the second prizes at provincial and ministerial level.

GUODONG LIU received the B.S. degree in mechanical design, manufacturing and automation from Ludong University, Yantai, China, in 2019. He is currently pursuing the M.S. degree with the Transportation and Vehicle Engineering School, Shandong University of Technology, Zibo, China.

His research interests include vehicle engineering, automotive electronics, design and manufacture of motor, and new energy electric vehicle technology.